

Start-to-end commissioning simulation for the HALF storage ring*

Ke-Min Chen,¹ Zhe Wang,¹ Tao He,¹ Duo-Hui He,¹ and Wei Xu^{1,†}

¹National Synchrotron Radiation Laboratory, University of Science and Technology of China, Hefei 230026, China

Hefei advanced light facility (HALF) is a 4th-generation diffraction-limited synchrotron light source which started construction in 2023. The storage ring has an extremely low emittance of less than $100 \text{ pm} \cdot \text{rad}$ with an energy of 2.2 GeV. It contains 20 superperiods of the modified hybrid 6-bend achromat with a circumference of about 480 m. A real storage ring is different from the ideal model due to various sources of errors, such as misalignment of components, imperfect magnetic fields, RF cavities, etc. As a result of strong nonlinear effects and small dynamic apertures, the errors have a serious effect on the low-emittance storage ring, which brings great difficulties to its commissioning. To figure out the practical performance of the machine with those errors, the start-to-end commission simulation is performed in this study, which also helps to verify the effectiveness of the commissioning of the HALF storage ring. In addition, the commissioning simulation process provides the basis for the development of the commissioning software for the HALF storage ring. Details and results of the commissioning simulation are reported in this paper.

Keywords: HALF, Storage ring, Commissioning simulation, Beam-based alignment, LOCO.

I. INTRODUCTION

The synchrotron radiation source has many advantages such as high intensity, high brightness, transverse coherence, good time structure, very broad and continuous spectral range, etc [1]. Since the 1970s, dedicated synchrotron radiation light sources have been developed as one of the most powerful scientific research tools over decades [2]. The 2nd-generation light sources use synchrotron from bending magnets while for the 3rd-generation light sources, the insertion devices (IDs) become the dominant radiation sources [3–5]. The 4th-generation synchrotron radiation light sources are proposed in recent years [6]. By reducing the emittance of the electron beam in the storage ring, the brightness and coherence of the diffraction-limited synchrotron radiation (DLSR) are increased by two to three orders of magnitude compared with the 3rd-generation light sources [7, 8]. This huge and qualitative leap greatly enhances the research capacity of synchrotron radiation [9]. MAX-IV is the first 4th-generation light source which employs the Multi-bend Achromat (MBA) lattice for its storage ring [10]. Since then several other 4th-generation light sources have been built or upgraded from old ones around the world [11–14].

High Energy Photon Source (HEPS) is the first 4th-generation light source in China, which is under commissioning at present [15, 16]. Southern advanced photon source (SAPS) is a mid-energy DLSR light source which is at its design stage [17]. Recently, an upgrade plan is proposed to turn Shanghai Synchrotron Radiation Facility (SSRF) to a soft X-ray diffraction-limited source (SSRF-U) [18–20]. Hefei Advanced Light Facility (HALF) is a 4th-generation light source that has been under construction since 2023 [21, 22]. The HALF storage ring contains 20 superperiods with modified hybrid 6-bend achromat with an emittance of less than $100 \text{ pm} \cdot \text{rad}$. The goal of the HALF project is to build a high-

performance synchrotron radiation light source in the VUV to soft X-ray region.

In a 4th-generation light source storage ring, the quadrupoles with strong strengths are used in order to obtain a low emittance, which results in the large negative chromaticities. To correct the chromaticities, intense sextupoles are adopted, leading to strong nonlinearity [23]. Due to the strong quadrupoles and sextupoles, the magnetic field feed-down effects of the off-axis beam are also large. Therefore, the errors of the machine components can severely affect the linear optics and dynamic performance of the storage ring. Besides, the dynamic aperture of the ultra-low emittance storage ring is much smaller than that of the 3rd-generation ring, which causes additional difficulties to its commissioning [24]. Therefore, the simulated commissioning for a 4th-generation light source storage ring is essential before the commissioning of the real machine [25, 26]. A preliminary study on the simulated commissioning for the HALF storage ring is reported in a previous paper [27]. To figure out the performance of the storage ring and verify the effectiveness of the correction to various errors, the start-to-end simulated commissioning is performed and reported in this paper. The simulated correction process is also the basis for the online commissioning of the HALF storage ring in the future. A recently developed Commissioning Simulation toolkit (SC) [28] based on the commonly used Accelerator Toolbox (AT) [29] is adopted in this study.

The subsequent sections of this paper are organized as follows. In Sect. II, the basic performance and layout of the HALF storage ring are introduced. In Sect. III, settings of various errors are given. The performance of the storage ring without any correction is shown in Sect. IV. In Sect. V, the correction chain of the simulated commissioning process is shown. Finally, the summary and conclusion are given in Sect. VI.

* Supported by the National Natural Science Foundation of China (No.11975227)

† Corresponding author, wxu@ustc.edu.cn

II. THE HALF STORAGE RING

A. Lattice

The modified hybrid 6-bend achromat lattice structure is adopted by the HALF storage ring in order to obtain an ultra-low emittance [30, 31]. The natural emittance is $85.8 \text{ pm} \cdot \text{rad}$ with an energy of 2.2 GeV . The ring is composed of 20 identical cells which provides 20 long and 20 short straight sections. The optic functions and layout of the lattice is shown in Fig. 1. The unit cell contains 6 dipoles, 4 reverse bends, 16 quadrupoles, 8 sextupoles and 2 octupoles. All dipole magnets are longitudinal gradient bending (LGB) magnets which help to reduce the nature emittance along with the reverse bends. The quadrupoles are powered independently in order to tune the optic functions. The sextupoles are used to correct the chromaticities and optimize the dynamic performance. To save space, the slow orbit correctors and skew quadrupole components are combined to those sextupoles. The main parameters of the HALF storage ring are shown in Table 1.

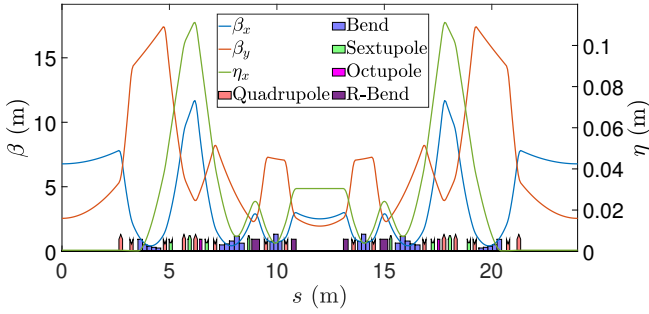


Fig. 1. (Color online) Optic functions of the HALF storage ring in one unit cell.

Table 1. Main parameters of the HALF storage ring.

Parameter	Value	Unit
Energy	2.2	GeV
Circumference	479.86	m
RF frequency	499.8	MHz
Harmonic number	800	-
Natural emittance	85.8	$\text{pm} \cdot \text{rad}$
Transverse tunes	48.19/17.19	-
Natural Chromaticities	-81.6/-56.6	-
Corrected Chromaticities	+3/+3	-
Momentum compaction factor	9.4×10^{-5}	-
Damping partition number	1.36/1.00/1.64	-
Damping time	28.5/38.8/23.7	ms
Bunch length	1.32	mm
Natural energy spread	0.61×10^{-3}	-
Energy loss per turn	181.4	KeV
Synchrotron frequency	2.06	kHz
Linear energy acceptance	8.14	%

B. Dynamic performance

The HALF storage ring is carefully designed to optimize its dynamic performance. The on-momentum 4D and 6D dynamic apertures (DA) of the HALF storage ring are shown in Fig. 2, which are about 13 mm and 8 mm in the horizontal plane respectively. Benefiting from the relatively large DA, the off-axis injection scheme can be adopted, while it still causes difficulties to the ring commissioning. The local momentum aperture (LMA) is shown in Fig. 3, which is obtained by 6D tracking.

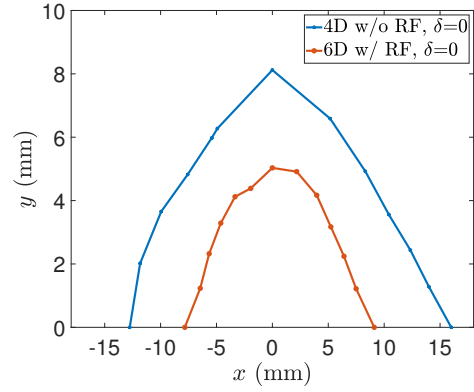


Fig. 2. (Color online) On-momentum dynamic aperture of the HALF storage ring.

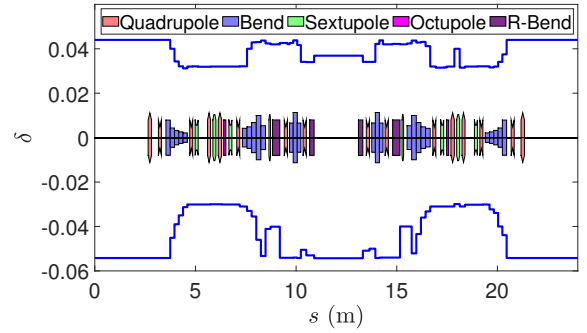


Fig. 3. (Color online) Local momentum aperture of the HALF storage ring.

C. Configuration of monitors and correctors

The configuration of the correctors and the beam position monitors (BPMs) is shown in Fig. 4. Each cell contains 12 horizontal and vertical orbit correctors and 12 BPMs. Among those correctors, 8 are combined to the multi-function sextupoles, and 4 isolated correctors are located at the ends of the straight sections. Skew quadrupole coils are combined to the sextupole families SD1, SD2 and SF1 in order to correct the coupling induced by the misalignment of the magnets. Since

the main vacuum chamber is a circular one with a diameter of 26 mm, a physical aperture with a radius of 13 mm is set to all elements.

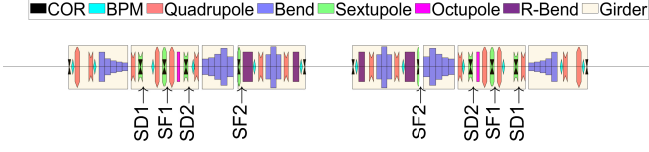


Fig. 4. (Color online) The configuration of correctors and BPMs in one unit cell.

III. ERROR SETTINGS

Before the commissioning simulation process, we need to incorporate various types of errors into the lattice to imitate the real machine. The random errors are generated based on a 2σ -truncated Gaussian distribution, where σ represents the root mean square (RMS) of the errors.

A. Misalignment and magnetic field errors

The misalignment and field errors of the main magnets are detailed in Table 2. In a real machine, magnets are installed on the girders. The magnets have misalignment errors while the girders also have misalignment errors. Therefore, the overall misalignment of the magnets are the sum of their own errors combined with the girder errors. The fields of the bends and quadrupoles are set with a 5×10^{-4} RMS fractional error. And the field errors of other multipoles are set to 1×10^{-3} .

B. BPMs and correctors

The resolution of the BPM turn by turn (TBT) data is set to $1 \mu\text{m}$, and the resolution for the closed orbit slow acquisition (SA) data is set to $0.1 \mu\text{m}$. A calibration error of the sum signal of 3% is assumed. The maximum strength of the orbit correctors is 1 mrad in both horizontal and vertical planes. To correct the ring coupling, skew quadrupoles with a maximum strength of 0.27 m^{-2} are adopted. The parameters of the BPMs and correctors are shown in Table 3.

C. RF errors

The errors of the RF system include the frequency, voltage and phase errors, which majorly comes from calibration, system shifting, closed orbit error and beam energy error of the storage ring, etc. The error information of the RF cavity can be obtained with beam transmission. The initial phase error of the RF cavity is usually large. The errors of the RF system are presented in Table 4.

D. Injection errors

As a 4th-generation light source, the HALF storage ring has a relatively large dynamic aperture, which greatly improves the ring acceptance and offers the possibility of using the off-axis injection scheme. The injection system of the HALF storage ring adopts the pulsed nonlinear kicker (NLK) method [32, 33], which is simple in structure and has little disturbance to the stored beam. By using the pulsed NLK, the injected bunch is directly kicked into the phase space within the acceptance of the storage ring. The injected beam is then damped onto the closed orbit of the stored beam after several damping times. The stored beam, which goes through the central field-free region, has a little impact from the NLK, making the injection transparency for the light source users.

A full-energy linac with an energy of 2.2 GeV is used as the injector of the storage ring. The injected beam from the linac has an emittance of $500 \text{ pm} \cdot \text{rad}$. The NLK along with a septum is located in one straight section, forming the whole injection system. The parameters of the injected beam at the injection position are shown in Tables 5, and the errors are described in Table 6.

IV. PERFORMANCE BEFORE CORRECTION

To figure out the difference between the ideal lattice and the actual one with errors, the performance of the HALF storage ring is studied before any correction. In a 4th-generation light source, the closed orbit (CO) may be absent without correction. The existence of the CO is investigated by scaling the global error factor as depicted in Fig. 5. It shows that the CO exists when the scaling factor is less than 20%. As the factor increases to 100%, the existence possibility of the CO decreases to less than 20%. The deviation of the CO as a function of the global error factor is shown in Fig. 6. We can see that as the global error factor increases, the deviation increases until the closed orbit is lost. When the factor increases to a certain level, the orbit deviation reaches its maximum before the beam is lost.

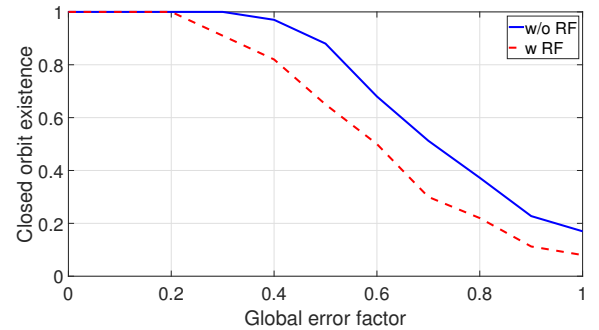


Fig. 5. (Color online) The closed orbit existence before any correction. The closed orbit exists when the scaling factor is less than 20%. As the factor increases to 100%, the existence possibility of the CO decreases to less than 20%.

Table 2. Misalignment errors and field errors for the main magnets and girders. dx , dy , and ds represent the shift errors in the horizontal, vertical, and longitudinal plane respectively. rx , ry , and rs denote the rotation errors around the horizontal, vertical, and longitudinal axis respectively.

Element	$dx(\mu\text{m})$	$dy(\mu\text{m})$	$ds(\mu\text{m})$	$rx(\mu\text{rad})$	$ry(\mu\text{rad})$	$rs(\mu\text{rad})$	Field
Bends	200	200	150	200	200	100	5×10^{-4}
Quadrupoles	30	30	150	100	100	100	5×10^{-4}
Sextupoles	30	30	150	100	100	100	1×10^{-3}
Octupoles	30	30	150	100	100	100	1×10^{-3}
Girder	100	100	200	100	100	100	-

Table 3. Errors of the BPMs and corrector magnets.

Parameter	Value	Unit
BPM noise for TBT	1	μm
BPM noise for CO	0.1	μm
BPM calibration error	3	%
BPM offset	200	μm
BPM roll around s -axis	100	μrad
BPM gain	5	%
CM calibration error	5	%
CM strength limit	1	mrad
CM offset	200	μm
CM roll	200	μrad
Skew quadrupole strength limit	0.27	m^{-2}
Skew quadrupole calibration error	5×10^{-4}	-

Table 4. RF cavity errors.

Parameters	Values	Units
Voltage offset	1	%
Frequency offset	1×10^3	Hz
Time lag offset	90	Deg

Table 5. Parameters of the injected beam.

Parameters	Values	Units
ϵ_x/ϵ_y	500/500	$\text{pm} \cdot \text{rad}$
σ_x	58.18	μm
$\sigma_{x'}$	8.59	μrad
σ_y	35.70	μm
$\sigma_{y'}$	14.01	μrad
σ_δ	0.05	%
σ_ϕ	15	ps

Table 6. Errors of the injected beam.

Parameters	Systematic	Jitter	Units
Δx	100	10	μm
$\Delta x'$	100	10	μrad
Δy	100	1	μm
$\Delta y'$	100	1	μrad
$\Delta E/E$	5×10^{-4}	1×10^{-4}	-
$\Delta\phi$	0	0.1	Deg

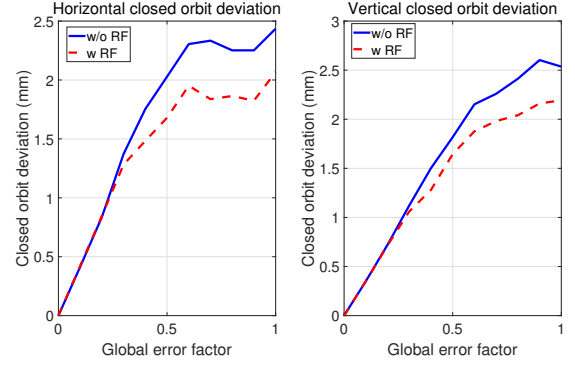


Fig. 6. (Color online) Deviation of the closed orbit as a function of the error scaling factor.

V. SIMULATED COMMISSIONING FOR THE HALF STORAGE RING

In this section, the correction chain of the simulated commissioning for the HALF storage ring is presented, which includes: A) Initial transmission correction (the first-turn trajectory correction and second-turn trajectory correction), B) Trajectory beam-based alignment, C) Injection correction, D) Sextupole ramping, E) RF correction, F) Beam-based alignment and G) Optics correction. In order to avoid the influence of the sextupoles and RF system on the beam dynamics, we turn them off at the beginning of commissioning.

A. Initial transmission

The beam usually fails to form a closed orbit and even can not pass through a complete turn in many cases at the beginning of the ring commissioning. To obtain the first-turn beam, the trajectory response matrix of the ideal lattice is used to perform trajectory correction at the BPMs which have turn-by-turn beam position signals. The correction process is repeated to let more BPMs have position signals. If the iteration yields no effect, the injected beam is scanned and the kick strengths of the correctors before the failure position are tuned until the beam passes through this BPM [34]. After the first-turn trajectory correction, the particles are expected to travel tens of turns. To further improve transmission of the beam, the trajectory of the second turn is corrected to be close to the first one. After the second-turn trajectory correc-

tion, more turns are expected to be achieved by the injected particles. The cumulative distribution functions (CDFs) of the beam loss under the first-turn and second-turn trajectory corrections are shown in Fig. 7.

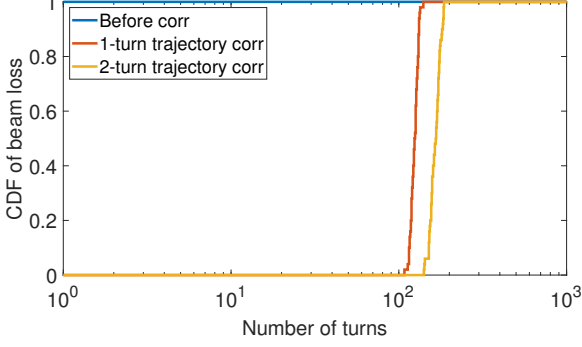


Fig. 7. (Color online) The cumulative distribution function of the beam loss after the first-turn and second-turn trajectory corrections.

B. Trajectory beam-based alignment

Due to the magnetic field feed-down effect, the electron beam would receive a kick when it travels away from the center of the quadrupoles. This additional kick has a significant impact on the beam transmission, especially for the low-emittance storage rings adopting the quadrupoles with strong strengths. To avoid this effect, the beam should pass through the centers of all quadrupoles. The beam-based alignment (BBA) technique is used to determine the center of a quadrupole by using a nearby BPM and the orbit correctors. The beam position $\mathbf{X}(s_0)$ (trajectory or orbit) of the particles at the quadrupole position s_0 can be described by

$$\mathbf{X}(s_0) = x_0 \hat{x} + y_0 \hat{y}, \quad (1)$$

where x_0 and y_0 are particle offsets relative to the quadrupole magnet center in the horizontal and vertical plane respectively.

Due to the feed-down effect, this quadrupole can generate a dipole field,

$$B_x = B_0 \rho_0 K y_0, \quad (2)$$

$$B_y = B_0 \rho_0 K x_0, \quad (3)$$

where $B_0 \rho_0$ is the magnetic rigidity, K is the normalized quadrupole strength.

By changing the quadrupole strength with ΔK , the variation of the dipole field is given by

$$\Delta B_x = B_0 \rho_0 \Delta K y_0, \quad (4)$$

$$\Delta B_y = B_0 \rho_0 \Delta K x_0. \quad (5)$$

For the closed orbit scenario, this variation results in an orbit change at location s [35],

$$\Delta \mathbf{X}(s) = \Delta K \mathcal{T}(s, s_0) \mathbf{X}(s_0), \quad (6)$$

$$\begin{aligned} \mathcal{T}(s, s_0) = & \left(\frac{1}{1 - K_0 \frac{L_0 \beta(s_0)}{2 \tan(\pi \nu)}} \right) \\ & \times \frac{\sqrt{\beta(s) \beta(s_0)}}{2 \sin(\pi \nu)} \cos(|\phi(s) - \phi(s_0)| - \pi \nu), \end{aligned} \quad (7)$$

where L_0 is the length of the quadrupole, $\beta(s_0)$ and $\beta(s)$ are the beta functions at the location of the quadrupole and the observation point respectively. $\phi(s_0)$ and $\phi(s)$ are the betatron phases, and ν is the betatron tune.

The function $\mathcal{T}(s, s_0)$ is related with the Courant-Snyder (C-S) parameters, which can be considered as a constant when the change of quadrupole strength ΔK is small. Then, the orbit change $\Delta \mathbf{X}(s)$ would be proportional to the orbit offset $\mathbf{X}(s)$. If the beam goes through the center of the quadrupole, the orbit change should theoretically be equal to zero. Using this principle, the quadrupole center can be obtained through measuring the orbit changes by varying the beam position in this quadrupole with a change in its strength ΔK [36]. If the beam orbit is least affected by changing the strength of the target quadrupole, the nearest BPM reading is considered as the center of the quadrupole.

The BBA process can also be applied to the trajectory case. The difference is that for the trajectory BBA, the beam position change is generated by adjusting the initial condition of the injected beam. After the trajectory BBA, the CDF of the beam loss is shown in Fig. 8, where an improvement in the beam transmission is seen.

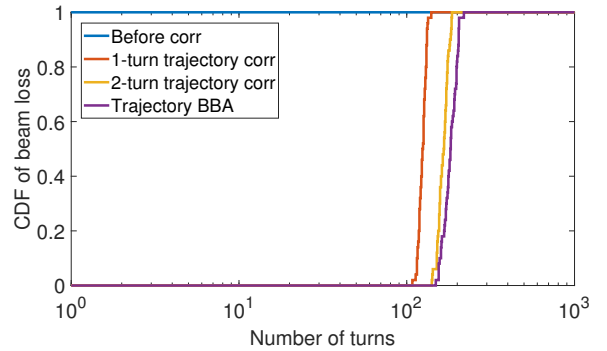


Fig. 8. (Color online) The cumulative distribution function of the beam loss after trajectory BBA.

C. Injection correction

To correct the static injection error, the injection correction is needed to obtain a better choice of the injection position.

In Fig. 9, the 1st-turn BPM readings in the upstream and 2nd-turn BPM readings in the downstream of injection position

are (x_u, y_u) and (x_d, y_d) , where $x_{u,d}$ and $y_{u,d}$ are the BPM reading in the horizontal and vertical planes respectively. And the distances between the BPM and injection position are l_u and l_d . Then the injection point can be moved the position,

$$x_{\text{inj}} = l_d \frac{x_u - x_d}{l_u + l_d} + x_d, \quad (8)$$

$$y_{\text{inj}} = l_d \frac{y_u - y_d}{l_u + l_d} + y_d, \quad (9)$$

and the injection angle is given by

$$x'_{\text{inj}} = \frac{x_d - x_u}{l_u + l_d}, \quad (10)$$

$$y'_{\text{inj}} = \frac{y_d - y_u}{l_u + l_d}. \quad (11)$$

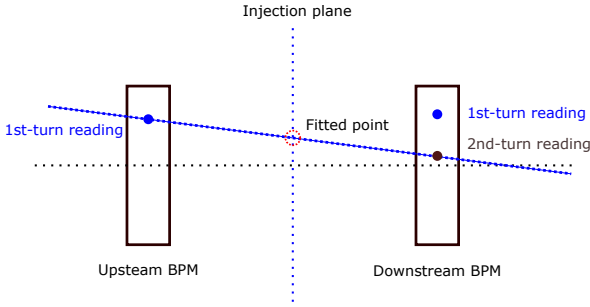


Fig. 9. (Color online) A schematic of the injection correction.

The CDF of the beam loss after the injection correction is shown in Fig. 10.

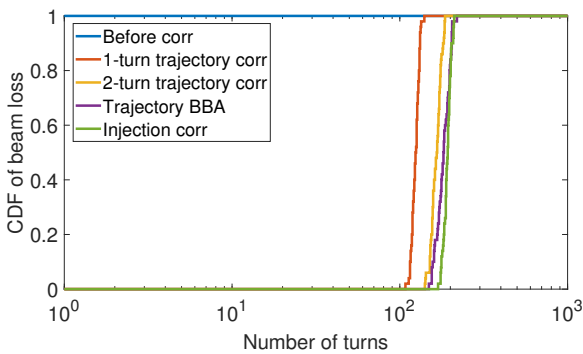


Fig. 10. (Color online) The cumulative distribution function of the beam loss after the injection correction.

D. Sextupole ramping

Due to the large nonlinear effect induced by the sextupoles, we turn them off at the beginning of the commissioning. For

a storage ring, the chromatic sextupoles are needed to correct the chromaticities to positive values in order to avoid the head-tail instability. Also the harmonic sextupoles are commonly adopted to optimize the dynamic performance of the storage ring. For sextupole ramping, the strengths of all sextupoles are increased in 5 steps. After each step, the trajectory is corrected to the reference trajectory obtained from the trajectory BBA. If necessary, the transverse tunes scan can be adjusted to improve the beam transmission. For a storage ring already in normal operation, a tune knob system can be developed to correct the tune while keeping the periodicity and maintain the global optics function [37]. Here at the commissioning stage, a simple way by using only two quadrupole families are adopted to scan the transverse tunes. Until now the synchrotron radiation of all magnets are on while the RF is turned off. The radiation loss per turn for a single particle is 181.4 keV. The linear energy acceptance of the HALF storage ring is 8.1%. This means the particles can travel about 987 turns ideally. In Fig. 11, we can see that the particles can go through near 600 turns, which shows an effective trajectory correction. Next we turn the RF on to form the closed orbit.

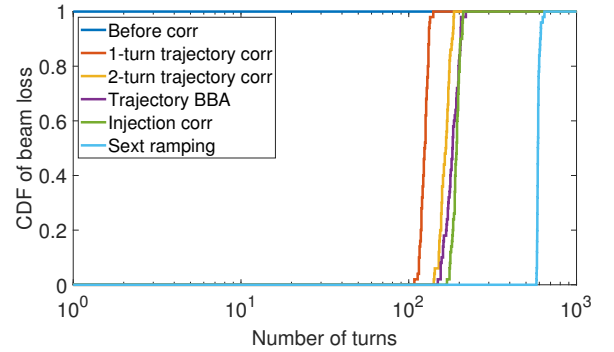


Fig. 11. (Color online) The cumulative distribution function of the beam loss after the sextupoles ramping.

E. RF correction

The BPM turn-by-turn (TBT) data can be used to correct the phase and frequency errors of the RF system. Due to the horizontal dispersion, the change of the horizontal beam position Δx induced by the energy variation ΔE is described as [38]

$$\frac{\Delta x}{\eta_x} = \frac{\Delta E}{E}, \quad (12)$$

where η_x is the horizontal dispersion, and E is the beam energy. The beam energy variation with the turn number n can be expressed as [39]:

$$\Delta E_n = eV \sin(\Delta\omega T_0 n + \varphi_0 + \Delta\varphi) - U_0, \quad (13)$$

where V is the rf voltage, φ_0 is the synchronous phase, T_0 is the synchronous period, U_0 is the radiation energy, $\Delta\omega$ and $\Delta\varphi$ are the frequency and phase errors.

By integrating Eq. 13 over the turn number n and combining with Eq. 12, the beam energy change after n turns is given by

$$\frac{\Delta x}{\eta_x} = \frac{E_n - E_0}{E} = -\frac{eV}{\Delta\omega T_0 E} [\cos(\Delta\omega T_0 n + \varphi_0 + \Delta\varphi) - \cos(\varphi_0 + \Delta\varphi)] - \frac{U_0 n}{E}. \quad (14)$$

Eq. 14 shows that the orbit variation is a function of the frequency error $\Delta\omega$ and phase error $\Delta\phi$. To correct the frequency and phase errors, we can adjust $\Delta\omega$ and $\Delta\phi$ to let Δx be 0. To simplify this procedure, we can do this correction separately.

For a real machine, the frequency error is usually small. To correct the phase error firstly, we assume $\Delta\omega$ to be 0. Then Eq. 14 turns out to be

$$\frac{\langle\Delta x\rangle}{\eta_x} = \frac{\Delta x}{n\eta_x} \approx \frac{eV}{E} \sin(\varphi_0 + \Delta\varphi) - \frac{U_0}{E}, \quad (15)$$

which shows that the average horizontal beam position variation $\langle\Delta x\rangle$ is a sine function of the rf phase φ_0 . After three iterations of the phase correction, the zero crossing is finally determined as the synchronous phase as shown in Fig. 12. To ensure at least 100 turns of beam transmission for the subsequent frequency correction, the tune scan is performed by changing the strengths of two quadrupole families after the first phase correction.

To correct the phase error $\Delta\phi$, $\Delta\omega T_0$ can be treated as a small quantity. Then Eq. 14 can be written as

$$\frac{\langle\Delta x\rangle}{\eta_x} = \frac{\Delta x}{n\eta_x} \approx \frac{eV}{E} \left[\frac{1}{2} \Delta\omega T_0 n \cos(\varphi_0 + \Delta\varphi) + \sin(\varphi_0 + \Delta\varphi) \right] - \frac{U_0}{E}, \quad (16)$$

where the average beam position variation $\langle\Delta x\rangle$ is a linear function of the frequency error $\Delta\omega$. A line is fitted and the zero crossing is considered as the synchronous frequency after three iterations as shown in Fig. 13.

In the RF correction, the synchrotron motion should be taken into consideration. The number of the evaluated turns should be significantly smaller than 304 turns for the HALF storage ring, which is related to the synchrotron frequency of 2.06 kHz. Therefore, the average position of 20 turns are adopted. The CDF of the beam loss is shown in Fig. 14. The beam can pass through more than 1000 turns and finally becomes a stored beam.

F. Beam-based alignment

In this step, the closed orbit BBA is performed in order to obtain the golden orbit. Recently a novel beam-based alignment method based on a neural network is developed to determine the beam reference orbit in a storage ring [40]. This method can be applied to the commissioning of the HALF storage ring in the future. For the simulation commissioning,

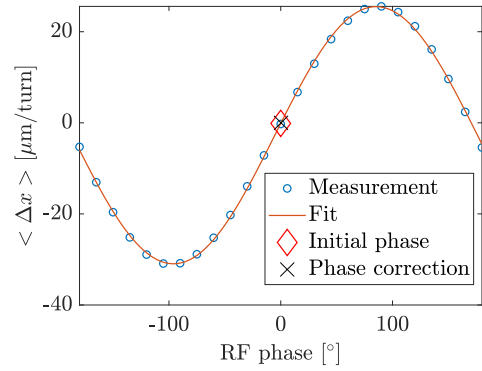


Fig. 12. (Color online) RF phase correction result in the final iteration.

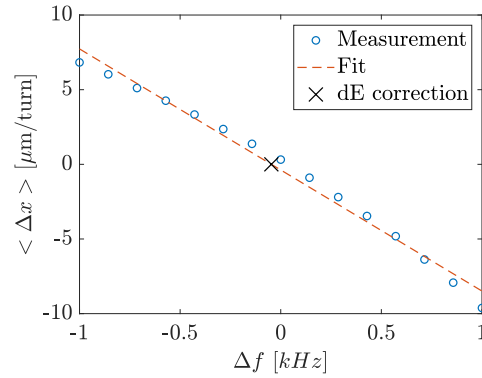


Fig. 13. (Color online) RF frequency correction result in the final iteration.

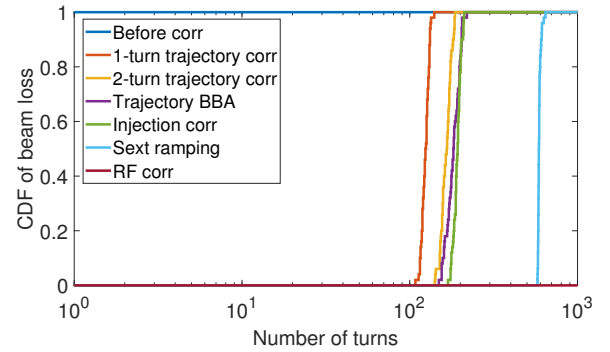


Fig. 14. (Color online) The cumulative distribution function of the beam loss after performing RF correction. The beam can be stored for more than 1000 turns.

the conventional method similar to the one mentioned in the previous subsection VB, except in the way of measuring the closed orbit is performed. In the CO BBA, we use the orbit correctors to generate different kick strengths on the beam to move the beam inside the target quadrupoles. After performing the CO BBA, the closed orbit is corrected to the reference orbit. After the orbit correction, the strengths of all correc-

tors with 10 sets of random error seeds are shown in Fig. 15. To mitigate the magnet feed-down effect, moving the beam to the quadrupole centers is critical for the optics correction.

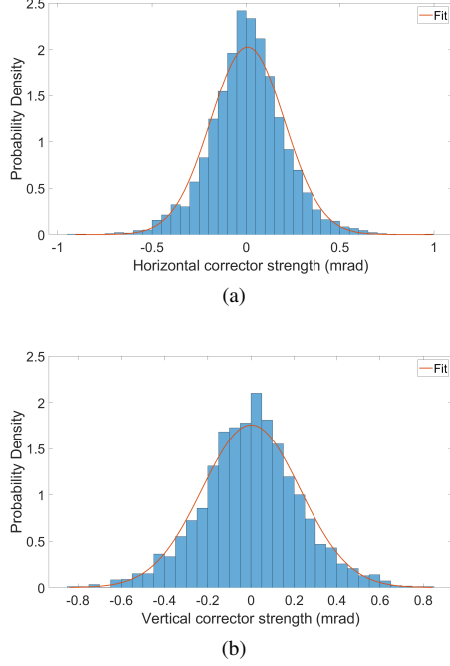


Fig. 15. Distribution of the corrector strengths after correcting the beam to the golden orbit: (a) Horizontal, (b) Vertical. The standard deviation of horizontal corrector strengths is 0.20 mrad, and the standard deviation of vertical corrector strengths is 0.23 mrad.

G. Optics correction

The linear optics is essential for the storage ring, which mainly includes the beta and dispersion functions [41]. Due to the lattice errors, the optics would deviate from their ideal values, which can result in the shifts of the betatron tunes, reduction of the dynamic aperture, etc. To correct the linear optics, a commonly used technique called the LOCO (Linear Optics from Closed Orbit) is performed, which can restore the periodicity of the storage ring, decrease the negative effects of nonlinear resonances, and increase the beam lifetime and DA [42, 43]. All quadrupoles are used for optics correction since they are powered independently. To correct the coupling, the skew quadrupole combined to the sextupole families SD1, SD2 and SF1 are used. The correction results for one error set are shown in Fig. 16 and Fig. 17. One can see that the beta beating and dispersion deviation is greatly reduced to a low level. The periodicity of the lattice is restored as shown in Fig. 18. The betatron tunes are (0.193, 0.195), which are close to the ideal values (0.190, 0.190).

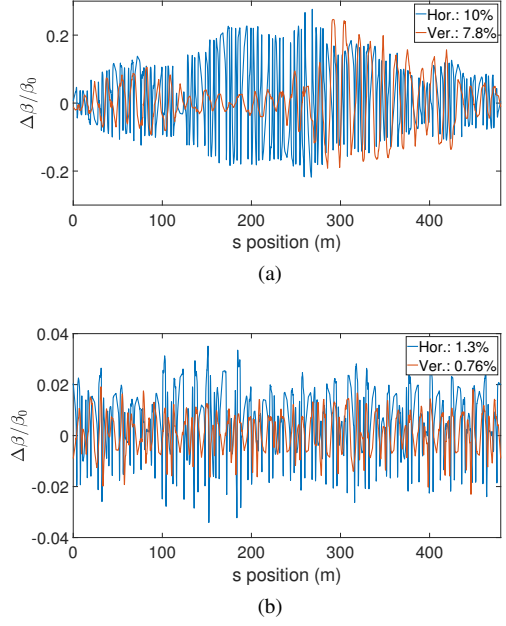


Fig. 16. Beta beating of the HALF storage ring before and after optics correction: (a) Before correction, (b) After correction. The horizontal beta beating (RMS) is reduced from 10% to 1.3% while the vertical beta beating is reduced from 7.8% to 0.76%.

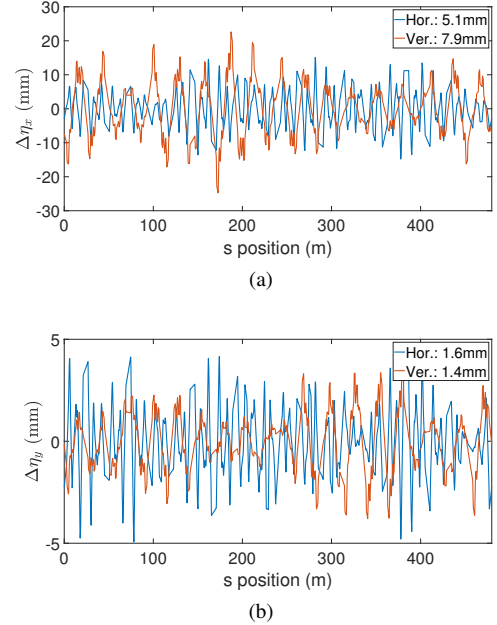


Fig. 17. Dispersion deviation of the HALF storage ring before and after optics correction: (a) Before correction, (b) After correction. The horizontal dispersion deviation (RMS) is reduced from 5.1 mm to 1.6 mm while the vertical dispersion deviation is reduced from 7.9 mm to 1.4 mm.

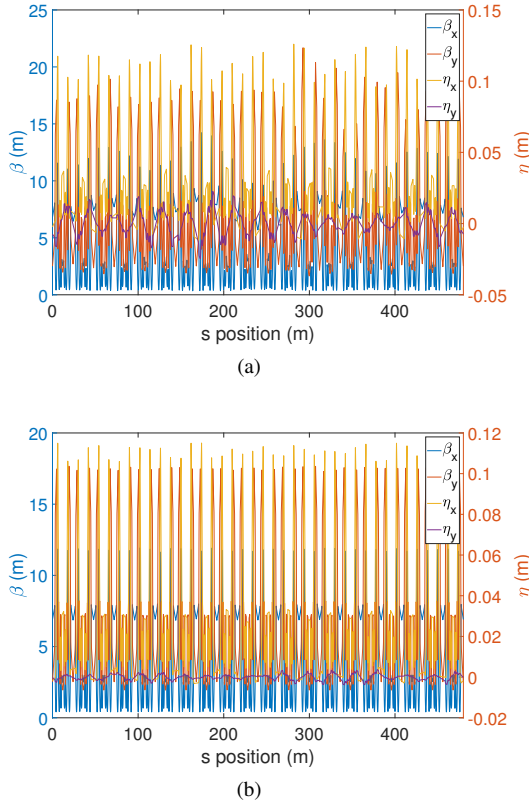


Fig. 18. Linear optics of the HALF storage ring before and after correction: (a) Before correction, (b) After correction. It is obvious that the periodicity of the lattice is restored.

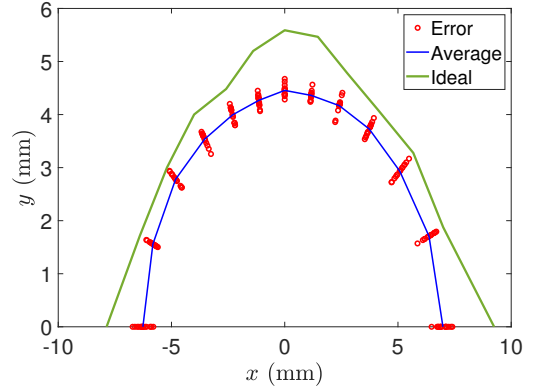


Fig. 19. (Color online) On-momentum 6D dynamic aperture of the HALF storage ring after correction.

VI. SUMMARY AND CONCLUSION

The start-to-end commissioning simulation for the HALF storage ring is performed. For this 4th-generation light source ring, the electron beam can not form the closed orbit with errors at the beginning of the commissioning. After a series of effective correction procedures, the beam is stored, and the optic functions of the lattice are corrected to the ideal model. To figure out the recovery of the dynamic performance of the storage ring, the start-to-end commissioning simulation is performed with 10 sets of random error seeds. After the correction, the 6D dynamic aperture of the ring is close to the ideal one, as is seen in Fig. 19. It shows that the whole correction chain presented above is effective and successful. It guarantees a significant increase of our confidence in commissioning the real machine in the future. Also the commissioning software is going to be developed based on this simulated commissioning.

- [1] S. Mobilio, F. Boscherini, and C. Meneghini, *Synchrotron Radiation: Basics, Methods and Applications* (Springer, 2015).
- [2] D. H. Bilderback, P. Elleaume, and E. Weckert, *Journal of Physics B: Atomic, Molecular and Optical Physics* **38**, S773 (2005).
- [3] H.-J. Xu and Z.-T. Zhao, *Nuclear Science and Techniques* **19**, 1 (2008).
- [4] S.-Q. Tian, B.-C. Jiang, Q.-G. Zhou, Y.-B. Leng, and Z.-T. Zhao, *Nuclear Science and Techniques* **25**, 010102 (2014).
- [5] Y.-Y. Wang, L. Shang, F.-L. Shang, and Y.-M. Lu, *Nuclear Science and Techniques* **27**, 2 (2016).
- [6] D. Einfeld, M. Plesko, and J. Schaper, *Journal of Synchrotron Radiation* **21**, 856 (2014).
- [7] S. C. Leemann, S. Liu, A. Hexemer, M. A. Marcus, C. N. Melton, H. Nishimura, and C. Sun, *Phys. Rev. Lett.* **123**, 194801 (2019).
- [8] R. Hettel, *Journal of Synchrotron Radiation* **21**, 843 (2014).
- [9] M. Eriksson, J. F. van der Veen, and C. Quitmann, *Journal of Synchrotron Radiation* **21**, 837 (2014).
- [10] P. F. Tavares, S. C. Leemann, M. Sjöström, and Å. Andersson, *Journal of Synchrotron Radiation* **21**, 862 (2014).
- [11] C. Steier *et al.*, in *Proceedings of IPAC'17*, International Particle Accelerator Conference No. 8 (JACoW, Geneva, Switzerland, 2017) pp. 2824–2826.
- [12] L. Liu, N. Milas, A. H. C. Mukai, X. R. Resende, and F. H. de Sá, *Journal of Synchrotron Radiation* **21**, 904 (2014).
- [13] J.C. Biasci, J.-F. Bouteille, N. Carmignani, J. Chavanne, D. Coulon, Y. Dabin, F. Ewald, L. Farvacque, L. Goirand, M. Hahn, J. Jacob, G. Lebec, S. M. Liuzzo, B. Nash, H. Pedroso-Marques, T. Perron, E. Plouviez, P. Raimondi, J. L. Revol, K. B. Scheidt, and V. Serrière, *Synchrotron Radiation News* **27**, 12 (2014).
- [14] M. Borland, T. Berenc, R. Lindberg, V. Sajaev, and Y. Sun, in *Proceedings of NAPAC'16*, North American Particle Accelerator Conference No. 3 (JACoW, Geneva, Switzerland, 2017) pp. 877–880.
- [15] Y. Jiao, G. Xu, X.-H. Cui, Z. Duan, Y. Guo, P. He, D. Ji, J. Li, X.-Y. Li, C. Meng, Y. Peng, T. Saike, J.-Q. Wang, N. Wang, Y.-Y. Wei, H. Xu, F. Yan, C.-H. Yu, Y.-L. Zhao, and Q. Qin,

- [Journal of Synchrotron Radiation](#) **25**, 1611 (2018).
- [16] Y.-M. Peng, J.-S. Cao, J.-H. Chen, H.-Y. Dong, P. He, Y. Jiao, L. Kang, W. Kang, J. Li, J.-Y. Li, G.-P. Lin, F. Liu, F.-L. Long, C. Meng, X. Qi, H.-M. Qu, Y.-F. Sui, S. Wang, G. Xu, Q. Ye, J. Zhang, P. Zhang, and W.-M. Pan, [Nuclear Science and Techniques](#) **35**, 16 (2024).
- [17] Y. Zhao, Y. Jiao, and S. Wang, [Nuclear Science and Techniques](#) **32**, 71 (2021).
- [18] Z. Zhao, B. Jiang, Y. Leng, S. Tian, L. Yin, and M. Zhang, in [Proceedings of IPAC'15](#), International Particle Accelerator Conference No. 6 (JACoW, Geneva, Switzerland, 2015) pp. 1672–1674.
- [19] X.-Z. Liu, S.-Q. Tian, X. Wu, M. Wang, and Z.-T. Zhao, [Nuclear Science and Techniques](#) **32**, 83 (2021).
- [20] X. Wu, S. Tian, X. Liu, W. Zhang, and Z. Zhao, [Nuclear Instruments and Methods in Physics Research Section A: Accelerators, Spectrometers, Detectors and Associated Equipment](#) **1025**, 166098 (2022).
- [21] Z. Bai, G. Feng, T. He, W. Li, W. Li, G. Liu, Z. Ren, L. Wang, P. Yang, S. Zhang, and T. Zhang, in [Proceedings of IPAC'21](#), International Particle Accelerator Conference No. 12 (JACoW Publishing, Geneva, Switzerland, 2021) pp. 407–409.
- [22] P.-H. Yang, G.-W. Liu, J.-H. Xu, W.-W. Li, T.-L. He, and Z.-H. Bai, [Nuclear Science and Techniques](#) **34**, 107 (2023).
- [23] H.-X. Yin, J.-B. Guan, S.-Q. Tian, and J.-K. Wang, [Nuclear Science and Techniques](#) **34**, 147 (2023).
- [24] W. Gao, L. Wang, and W. Li, [Phys. Rev. ST Accel. Beams](#) **14**, 094001 (2011).
- [25] D. Ji, X. Cui, Z. Duan, Y. Jiao, Y. Wei, and Y. Zhao, in [Proceedings of IPAC'18](#), International Particle Accelerator Conference No. 9 (JACoW Publishing, Geneva, Switzerland, 2018) pp. 4186–4188.
- [26] D. Ji, B. Wang, and X. Cui, in [Proceedings of IPAC'23](#), IPAC'23 - 14th International Particle Accelerator Conference No. 14 (JACoW Publishing, Geneva, Switzerland, 2023) pp. 492–495.
- [27] K. Chen, Z. Wang, G. Wang, T. He, Z. Wang, M. Hosaka, D. He, and W. Xu, in [Proceedings of IPAC'24](#), IPAC'24 - 15th International Particle Accelerator Conference No. 15 (JACoW Publishing, Geneva, Switzerland, 2024) pp. 2043–2045.
- [28] T. Hellert, P. Amstutz, C. Steier, and M. Venturini, [Phys. Rev. Accel. Beams](#) **22**, 100702 (2019).
- [29] A. Terebilo, in [Proceedings of PACS2001](#), Vol. 4 (2001) pp. 3203–3205 vol.4.
- [30] Z.-H. Bai, G.-W. Liu, T.-L. He, W.-W. Li, P.-H. Yang, W.-M. Li, S.-C. Zhang, L. Wang, and G.-G. Feng, [High Power Laser and Particle Beams](#) **34**, 104003 (2022).
- [31] Z. Bai, G. Feng, T. He, W. Li, W. Li, G. Liu, L. Wang, P. Yang, and S. Zhang, in [Proceedings of IPAC'23](#), IPAC'23 - 14th International Particle Accelerator Conference No. 14 (JACoW Publishing, Geneva, Switzerland, 2023) pp. 1075–1078.
- [32] G. Liu, W. Li, L. Wang, and P. Wang, in [Proceedings of IPAC'21](#), International Particle Accelerator Conference No. 12 (JACoW Publishing, Geneva, Switzerland, 2021) pp. 2878–2880.
- [33] W. Song, L. Shang, F. Shang, W. Liu, and Z. Sun, [Nuclear Instruments and Methods in Physics Research Section A: Accelerators, Spectrometers, Detectors and Associated Equipment](#) **990**, 164986 (2021).
- [34] S. Liuzzo, N. Carmignani, L. Farvacque, and B. Nash, in [Proceedings of IPAC'17](#), International Particle Accelerator Conference No. 8 (JACoW, Geneva, Switzerland, 2017) pp. 3067–3070.
- [35] G. Portmann, D. Robin, and L. Schachinger, in [Proceedings of Particle Accelerator Conference](#), Vol. 4 (1995) pp. 2693–2695 vol.4.
- [36] X. Huang, [Beam-based Correction and Optimization for Accelerators](#), 1st ed. (CRC Press, Boca Raton, 2019).
- [37] S.-W. Wang, W. Xu, X. Zhou, W.-B. Wu, B. Li, K. Xuan, and J.-Y. Li, [Nuclear Science and Techniques](#) **29**, 176 (2018).
- [38] S.-Y. Lee, [Accelerator Physics Fourth Edition](#) (World Scientific Publishing Company, 2018).
- [39] V. Sajaev, [Phys. Rev. Accel. Beams](#) **22**, 040102 (2019).
- [40] G.-L. Wang, K.-M. Chen, S.-W. Wang, Z. Wang, T. He, M. Hosaka, G.-Y. Feng, and W. Xu, [Nuclear Science and Techniques](#) **35**, 75 (2024).
- [41] G. Liu, L. Wang, F. Wu, and K. Xuan, in [Proceedings of IPAC'17](#), International Particle Accelerator Conference No. 8 (JACoW, Geneva, Switzerland, 2017) pp. 727–729.
- [42] J. Safranek, [Nuclear Instruments and Methods in Physics Research Section A: Accelerators, Spectrometers, Detectors and Associated Equipment](#) **388**, 27 (1997).
- [43] G. J. Portmann, J. A. Safranek, and X. Huang, [MATLAB-BASED LOCO](#), Tech. Rep. (SLAC National Accelerator Lab., Menlo Park, CA (United States), 2011).